AIAA JOURNAL
Vol. 49, No. 4, April 2011

Improved Low-Reynolds-Number One-Equation Turbulence Model

M. M. Rahman* and T. Siikonen*
Aalto University, FI-00076 AALTO, Finland
and
R. K. Agarwal†
Washington University, St. Louis, Missouri 63130

DOI: 10.2514/1.J050651

A low-Reynolds-number extension of the Baldwin–Barth one-equation turbulence model is proposed and evaluated. The eddy viscosity damping function f_μ invokes an elliptic relaxation approach to account for the distinct effects of low Reynolds number and wall proximity. The k and ϵ, which render the undamped eddy viscosity, are evaluated using the $R(=k^2/\epsilon)$ transport equation together with the Bradshaw and other empirical relations. The model coefficients/functions preserve the anisotropic characteristics of turbulence in the sense that they are sensitized to nonequilibrium flows. The model is validated against a few well-documented flow cases, yielding predictions in good agreement with the direct numerical simulation and experimental data. The R-transport equation having two different source terms replicates almost analogous results. Comparisons indicate that the present model offers considerable improvement over the modified Spalart–Allmaras one-equation model and competitiveness with the shear stress transport k-ω model.

Nomenclature

b_{ij}	=	Reynolds stress anisotropy
C_f	=	friction coefficient
C_p	=	pressure coefficient
C_μ	=	eddy viscosity coefficient
f_μ	=	viscous damping function
h	=	channel/step height
k	=	turbulent kinetic energy
L	=	characteristic length scale
P	=	production of turbulent kinetic energy
R	=	fictitious eddy viscosity
$\tilde{R}$	=	undamped eddy viscosity
Re	=	Reynolds number
S	=	mean strain rate
T_t	=	realizable time scale
t	=	time
u_τ	=	friction velocity
$-\overline{uv}$	=	shear stress
W	=	mean vorticity
y^+	=	nondimensional normal distance from the wall
δ	=	half-width of the channel
δ_{ij}	=	Kronecker's delta
ϵ	=	turbulent dissipation
ζ	=	strain rate/vorticity parameter
μ, μ_T	=	laminar and eddy viscosities
ν	=	molecular kinematic viscosity
Π_b	=	turbulent anisotropy
ρ	=	density
σ	=	turbulent Prandtl number

Subscripts

ref	=	reference condition
T	=	turbulent condition
w	=	wall condition

I. Introduction

A NUMBER of scientific and engineering calculations adhering to turbulent flows are established on one-equation models due to their simplicity of implementation and less demanding computational requirements, compared with the standard two-equation k-ϵ and k-ω models. The algebraic model such as Baldwin–Lomax model [1] is efficient from a numerical point of view but lacks generality for not having transport and diffusion effects. However, one-equation models include transport effects and can be considered as a good compromise between algebraic and two-equation models.

Considerable research is devoted to improving the accuracy of one-equation models, comprising the equilibrium and nonequilibrium flows [2–7]. The Baldwin–Barth (BB) model [2] derived using the k-ϵ closure is among the first one-equation models to be self-consistent by avoiding the use of algebraic length scales. Nevertheless, in the course of transformation some other major assumptions are made that weaken the link with its parent k-ϵ models. As a result, the BB model performs very differently from the underlying k-ϵ model, even in simple equilibrium flows [4]. To a larger extent, the failure of the BB model lies in the destruction term. Besides, it is sensitive to the freestream value of the turbulent Reynolds number and yields unexpected results in predicting the separation in attached flows with mild to strong adverse pressure gradients. In addition, the diffusive term that is not directly connected to the k-ϵ model renders the model ill-conditioned in the shear layer regions. However, the BB model has good near-wall benign properties like the linear behavior of its transport property, which in turn does not require a finer grid than an algebraic model does [5]. Spalart and Allmaras (SA) [3] derive their model using empiricism and arguments of dimensional analysis, having no link to the k-ϵ equations. The motivation for this approach is that the BB model is constrained by assumptions inherited from the k-ϵ model.

In principle, Menter [4], in his transformation from the k-ϵ closure to the one-equation model shows a closer connection than the BB model using the Bradshaw relation (see [8]; i.e., the shear stress in the boundary layer is proportional to the turbulent kinetic energy).

Received 10 May 2010; revision received 12 November 2010; accepted for publication 4 December 2010.

*School of Science and Technology, Department of Applied Mechanics, PO Box 14400.

†School of Science and Technology, Department of Mechanical, Aerospace, and Structural Engineering.

Menter also mentions that using the Bradshaw relation seems to be more effective in nonequilibrium flows. However, transforming the k-ϵ closure may carry many of its deficiencies, such as the bad performance in wall-bounded flows in the presence of mild adverse pressure gradients. Further modifications to one-equation models based on the use of Bradshaw relation are proposed in [5–7] that account for near-wall turbulence, providing good results for simple/complex flows with separation and reattachment.

The present study advances with resorting to near-wall and low-Reynolds-number (LRN) modifications for the BB model where the integration up to the wall is extremely important. This version has several desirable attributes relative to the original BB model:

1) It revives the link between the BB and k-ϵ models via the source/sink and diffusion terms, using the turbulence structure parameter $a_1 = |-\overline{uv}|/k$ (Bradshaw relation).

2) The use of an equilibrium between production and dissipation leads to two different source terms (i.e., two one-equation models), allowing a cross comparison of the impact of different source terms on the performance of one-equation closures.

3) An elliptic relaxation function f_μ, the length scale of which is explicitly influenced by the mean flow and turbulent variables, is devised to suppress the excessive eddy viscosity in near-wall regions.

4) It enforces time scale realizability by preventing it from falling below the Kolmogorov (dissipative eddy) scale.

5) The turbulent Prandtl number σ is adjusted such as to provide substantial turbulent diffusion in the near-wall region.

6) Source/sink term coefficients $C_{1,2}$ and C_μ, that depend nonlinearly on both the rotational and irrotational strains are proposed based on the realizability constraints and appropriate experiments. Consequently, the model extends the ability of the one-equation model to account for nonequilibrium and anisotropic effects, a feature that is missing in the single equation models developed so far. Ostensibly, the new model is tensorially invariant, frame-indifferent and applicable to arbitrary topologies.

The performance of the new model is demonstrated through the comparison with experimental and direct numerical simulation (DNS) data of well-documented flows, consisting of fully developed channel flows, a backward facing step flow, an asymmetric plane diffuser flow, and a plane U-duct flow, respectively. The test cases are selected such as to justify the ability of the model to replicate the combined effects of LRN, near-wall turbulence and nonequilibrium. Since the SA model is not transformed from the k-ϵ closure, it would be interesting to compare the present model predictions with those of the SA model.

II. Model Formulation

The principal assumption in deriving the one-equation model is that $|-\overline{uv}| \propto k$, which is equivalent to $P = \epsilon$ in standard two-equation k-ϵ models. The second assumption is that $\sigma = \sigma_k = \sigma_\epsilon$. A more detailed derivation can be found in [4]. In collaboration with the Reynolds-averaged Navier–Stokes equations, the proposed model determines $R = k^2/\epsilon$ (fictitious eddy viscosity) by the following transport relation. The one-equation turbulence model for high-Reynolds-number wall-bounded flows developed by Baldwin and Barth [2] is modified to evaluate R as

$$\frac{\partial \rho R}{\partial t} + \frac{\partial \rho u_j R}{\partial x_j} = \frac{\partial}{\partial x_j}\left[\left(\mu + \frac{\mu_T}{\sigma}\right)\frac{\partial R}{\partial x_j}\right] + C_1 \rho \sqrt{P\tilde{R}} - C_2 \rho \left(\frac{\partial \tilde{R}}{\partial x_k}\right)^2 \tag{1}$$

subjected to $R_w = 0$ at solid walls. Herein, ρ is the density, μ implies the molecular viscosity, σ is the appropriate turbulent Prandtl number, the production term $P = -\overline{u_i u_j}(\partial u_i/\partial x_j)$, and the undamped eddy viscosity $\tilde{R} = kT_t$. Compared with the original BB model, the new model replaces R by $\tilde{R}$ from μ_T (eddy viscosity/diffusion), C_1 (production) and C_2 (destruction) terms that renders the direct coupling among R, k and ϵ. The Reynolds stresses $\rho\overline{u_i u_j}$ are related to the mean strain rate tensor S_{ij} through the Boussinesq approximation:

$$-\rho\overline{u_i u_j} = 2\mu_T\left(S_{ij} - \frac{1}{3}S_{kk}\delta_{ij}\right) - \frac{2}{3}\rho k \delta_{ij}, \qquad S_{ij} = \frac{1}{2}\left(\frac{\partial u_i}{\partial x_j} + \frac{\partial u_j}{\partial x_i}\right) \tag{2}$$

Since the viscous dissipation presumably dominates near the wall, the turbulent viscosity is evaluated from

$$\mu_T = C_\mu f_\mu \rho \tilde{R} = C_\mu f_\mu \rho k T_t \tag{3}$$

where the dynamic time scale k/ϵ is replaced by a realizable time scale T_t defined as

$$T_t = \sqrt{\frac{k^2}{\epsilon^2} + C_T^2\frac{\nu}{\epsilon}} = \frac{k}{\epsilon}\sqrt{1 + \frac{C_T^2}{Re_T}}, \qquad Re_T = \frac{k^2}{\nu\epsilon} \tag{4}$$

where ν denotes the kinematic viscosity and Re_T is the turbulence Reynolds number. Equation (4) warrants that the eddy time scale never falls below the Kolmogorov time scale $C_T\sqrt{\nu/\epsilon}$, dominant in the immediate neighborhood of the solid wall. Alternatively, the turbulence time scale is k/ϵ at large Re_T but approaches the Kolmogorov limit $C_T\sqrt{\nu/\epsilon}$ for $Re_T \ll 1$. The empirical constant $C_T = \sqrt{2}$ associated with the Kolmogorov time scale is estimated from the behavior of k in the viscous sublayer [9].

In particular, the consequence of an equilibrium between production and dissipation (i.e., $P = \epsilon$) leads to the following compatibility relations:

$$\sqrt{P\tilde{R}} \approx PT_t \tag{5}$$

However, $P = \epsilon$ is not confirmed by experimental evidence in strong adverse pressure gradient flows. The inhomogeneity of turbulence is needed to affect the departure from equilibrium. The relation (1) can be recast as

$$\frac{\partial \rho R}{\partial t} + \frac{\partial \rho u_j R}{\partial x_j} = \frac{\partial}{\partial x_j}\left[\left(\mu + \frac{\mu_T}{\sigma}\right)\frac{\partial R}{\partial x_j}\right] + C_1 \rho S_\lambda - C_2 \rho \left(\frac{\partial \tilde{R}}{\partial x_k}\right)^2 \tag{6}$$

where $S_\lambda = (S_1 = \sqrt{P\tilde{R}}, S_2 = PT_t)$, signifying that the substitution of Eq. (5) into Eq. (1) gives rise to two one-equation models with different source terms. In this study, the internal consistency of this reconstruction is demonstrated through predictions of different flow types (i.e., simple and nonequilibrium flows). Equation (6) presents a closure problem for one-equation with three unknowns and therefore, in order to close it, k and ϵ are evaluated using the R-transport equation together with the Bradshaw (see [8]) and other empirical relations.

The eddy viscosity damping function f_μ in Eq. (3) is obtained by solving the elliptic f_μ equation that envisages LRN and wall proximity effects. The model coefficient C_μ is in general a scalar function of the invariants formed on the strain rate S_{ij} and vorticity W_{ij} tensors in question [10,11]. The vorticity tensor W_{ij} is defined as

$$W_{ij} = \frac{1}{2}\left(\frac{\partial u_i}{\partial x_j} - \frac{\partial u_j}{\partial x_i}\right) \tag{7}$$

The invariants of mean strain rate and vorticity tensors are defined by $S = \sqrt{2S_{ij}S_{ij}}$ and $W = \sqrt{2W_{ij}W_{ij}}$, respectively. The detailed functional form of C_μ is determined relying on the constraints such as realizability and appropriate experiments. The formulation of the model coefficients and associated relevant aspects are discussed in some detail in subsequent sections.

A. Coefficient C_μ

The new model appears with recourse to the realizability constraints, reflecting physically necessary conditions for developing a compatible turbulence model. The realizability conditions are defined as [12]

$$\bar{u}_i^2 \geq 0, \qquad \frac{\overline{u_i u_j}^2}{\overline{u_i^2}\,\overline{u_j^2}} \leq 1 \tag{8}$$

Equation (8) also represents the minimal requirement to prevent a turbulence model from producing nonphysical results. The commonly used isotropic eddy viscosity model with a constant $C_\mu = 0.09$ becomes unrealizable in the case of a large mean strain rate parameter $T_t S$ (when $T_t S > 3.7$), producing negative normal stresses in question and Eq. (8) is violated. To ensure realizability, the model coefficient C_μ cannot be a constant. It must be related with the mean flow deformation rate. Accordingly, a new formulation for C_μ as suggested by Gatski and Speziale [11] and Rahman and Siikonen [13] is adopted:

$$C_\mu = \frac{3(1+\eta^2)\alpha_1}{3+\eta^2+6\eta^2\xi^2+6\xi^2}, \qquad \eta = \alpha_2 T_t S, \qquad \xi = \alpha_3 T_t W \tag{9}$$

The coefficients α_1–α_3 associated with Eq. (9) are given by

$$\alpha_1 = g\left(\frac{1}{4}+\frac{2}{3}\Pi_b^{1/2}\right), \qquad \alpha_2 = \frac{3}{8\sqrt{2}}g$$
$$\alpha_3 = \frac{3}{\sqrt{2}}\alpha_2, \qquad g = \left(1+2\frac{P}{\epsilon}\right)^{-1} \tag{10}$$

where $\Pi_b = b_{ij}b_{ij}$ and the anisotropy of the Reynolds stress b_{ij} is defined as

$$b_{ij} = \frac{\overline{u_i u_j}}{2k} - \frac{1}{3}\delta_{ij} \tag{11}$$

Note that the constants associated with g are slightly modified to reproduce the data of DNS and experiments.

For homogeneous turbulent flows that are in equilibrium, Π_b and P/ϵ attain constant values, so that $\Pi_b \approx 0.11$ and $P/\epsilon \approx 1.9$. These values can be set in Eq. (10) to calculate inhomogeneous flows. However, the necessity to account for changes in Π_b and P/ϵ is appreciable since their equilibrium values drive the model to inconsistency in the context of a mild departure from equilibrium. To circumvent this problem in complex flows, compatible relations for Π_b and P/ϵ are devised that depend nonlinearly on both the rotational and irrotational strains [13]:

$$\Pi_b = C_v\frac{P}{\epsilon}, \qquad \frac{P}{\epsilon} = C_v\zeta^2 \tag{12}$$

with

$$C_v = \frac{1}{2(1+T_t S\sqrt{1+Re^2})}, \qquad \zeta = T_t S\max(1, Re) \tag{13}$$

where $Re = |W/S|$ is a dimensionless parameter that is very useful to characterize the flow. For instance, for a pure shear flow $Re = 1$, whereas for a plane strain flow $Re = 0$. It is appropriate to emphasize herein that the calibrated relations for Π_b and P/ϵ can assist the coefficients (α_1–α_3) in responding to both the shear and vorticity dominated flows that are far from equilibrium. Detailed analysis of the model realizability is available in [13].

B. Damping Function

The primary objective of introducing the damping function f_μ to turbulence models is to represent the kinematic blocking by the wall. Detailed analysis of DNS data shows that the wall blocking effect is much stronger than the viscous/LRN effect [14]. The empirical approach to modeling the wall blocking effect is often inconsistent with the complex flows and may degrade the results considerably. To eradicate the complexity in defining the wall distance with multiple surfaces, a Helmholtz-type elliptic relaxation equation for f_μ is introduced. It represents a general ellipticity pertaining to f_μ without the knowledge of the wall distance:

$$-L^2\nabla^2 f_\mu + f_\mu = 1 \tag{14}$$

where L is the characteristic length scale. To avoid the singularity close to the wall, the Kolmogorov length scale $(\nu^3/\epsilon)^{1/4}$ is generally added with the dynamic length scale $k^{3/2}/\epsilon$ [15]. In principle, the length scale L needs to be tuned consistently at the appropriate DNS/experimental data to evaluate the LRN/near-wall turbulence. Reference [16] shows that the Kolmogorov length scale plays an important role in modeling the near-wall turbulence. Therefore, L is constructed as a pure Kolmogorov length scale (i.e., excluding the dynamic/integral scale):

$$L^2 = \zeta(2\zeta + C_\mu Re_T)\sqrt{\frac{\nu^3}{\epsilon}} \tag{15}$$

where L contains a multiplying factor to fit the data, for instance, the DNS data for developed channel flows. Conspicuously, the strain rate/vorticity parameter associated with the Kolmogorov length scale in Eq. (15) reduces the large constant dependency of the relaxation function f_μ as mentioned by Durbin [15]. The rationale with the present approach is that the wall proximity effect is modeled naturally in conjunction with the elliptic relaxation function f_μ and hence nonlocal effects such as wall blocking. The virtue of Eq. (14) is that unlike the Poisson equation, it requires no special numerical treatment (i.e., the Laplace operator is relatively easy to treat, but particularly easy is the modification $-L^2\nabla^2 + 1$). It can be solved in parallel with the R equation having an initial guess $0 \leq f_\mu \leq 1$ everywhere except on wall boundaries where $f_\mu = 0$.

A plot of $C_\mu f_\mu$ against the DNS data [17] for fully developed turbulent channel flows is shown in Fig. 1 and good correlation is obtained. The elliptic function f_μ in Eq. (14) is valid in the whole

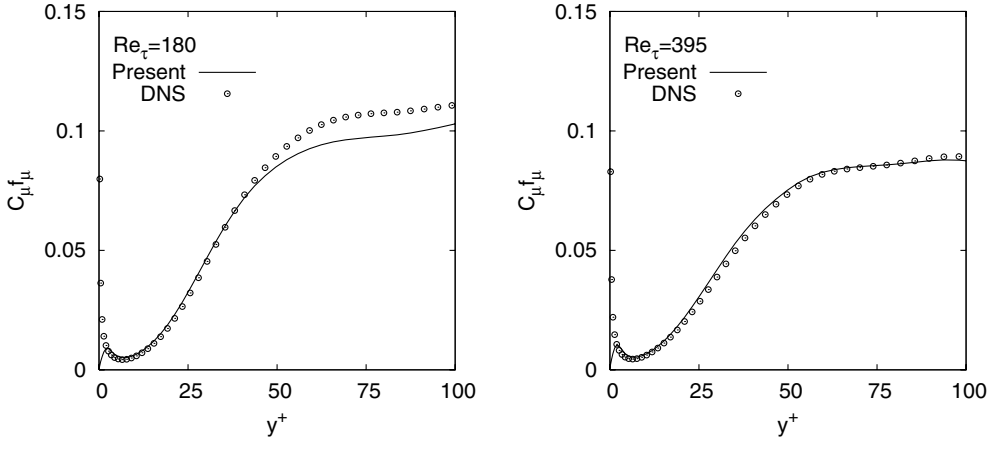

Fig. 1 Variations of eddy viscosity coefficient with wall distance in channel flow.

flow field, including the viscous sublayer and the logarithmic layer. As is evident by Fig. 1 in comparison with the DNS data, the adopted form of $C_\mu f_\mu$ reproduces the distinct effects of LRN and wall proximity. The product $C_\mu f_\mu \approx 0.09$ (the standard choice for $C_\mu = 0.09$, pertaining to the linear k-ϵ model) remote from the wall to ensure that the model is compatible with the high-Reynolds-number turbulence model. The use of elliptic relaxation function f_μ confronts the singularity at neither the separating nor the reattaching point in contrast to the adoption of $y^+ = u_\tau y/\nu$ (where u_τ is the friction velocity). Consequently, the model is applicable to separated and reattaching flows.

C. Other Model Coefficients

The model coefficients C_1 and C_2 are related to the k-ϵ constants by [2]

$$C_1 = C_{\epsilon 2} - C_{\epsilon 1} = 0.46, \qquad C_2 = (C_{\epsilon 2} - C_{\epsilon 1})\frac{\tilde{C}_\mu\sqrt{\tilde{C}_\mu}}{\kappa^2} \approx 0.08 \tag{16}$$

where $\kappa = 0.41$ is the von Kármán constant. The coefficients C_1 and C_2 are calculated based on the values of the standard k-ϵ closure where $C_{\epsilon 1} = 1.44$, $C_{\epsilon 2} = 1.92$ and $\tilde{C}_\mu = 0.09$. However, the necessity to account for changes in C_1 and C_2 is desirable in order to include the local anisotropy of turbulence as is practised in the k-ϵ turbulence model [16,18]. To explore the anisotropic situation, C_1 and C_2 are devised as a function of mean shear and vorticity parameters (i.e., $T_t S$ and $T_t W$, respectively):

$$\begin{aligned} C_1 &= 2\sqrt{\Pi_b^*}(1 - \sqrt{\Pi_b^*}), \\ C_2 &= \min\left[2C_\mu, \tilde{C}_\mu\sqrt{1 + \left(\frac{C_1}{6\tilde{C}_\mu}\right)^2}\right] \end{aligned} \tag{17}$$

where $\sqrt{\Pi_b^*} = C_\mu\zeta$ is essentially identical to Eq. (12), however, with the exception that C_v is replaced by C_μ. It can be stressed that the shear/vorticity parameter certainly induces compatible changes in $C_{1,2}$ which accounts for the anisotropy of turbulence. Remarkably, $C_1 \approx 0.42$ and $C_2 \approx 0.11$ in the log layer of a channel flow with $\zeta(Re = 1) \approx 3.3$. In principle, the reconstruction of $C_{1,2}$ assists qualitatively in predicting turbulent flows with separation and reattachment as shown in the computation section.

The budgets of k and ϵ from the DNS data suggest that the role of turbulent diffusion in the near-wall region is substantial. Accordingly, the Prandtl number σ is modeled, rather than being assigned constant value (unlike the commonly adopted practice with $\sigma \approx 1$):

$$\sigma = C_\mu + f_\mu/C_T \tag{18}$$

The model coefficients σ is developed so that sufficient diffusion is obtained in the vicinity of the wall. This contrivance tends to successfully predict the kinetic energy and dissipation rate profiles from the R-transport equation. Nevertheless, $C_\mu \approx 0.3$ and $f_\mu = 1.0$ in the freestream region and therefore, $\sigma \approx 1$ is recovered therein.

D. Determination of k and ϵ

The professed interest herein is to represent k and ϵ in the form of R. Probably, it is the most essential step, since the generality of the reconstructed k and ϵ must be guaranteed through a wide range of flows. The most appropriate assumption concerning such a reconstruction is the Bradshaw hypothesis (see [8]), implemented directly into many turbulence models [6]. With the Bradshaw relation, k may be expressed using $(C_\mu f_\mu^n R)$ through the turbulence structure parameter:

$$\frac{|-\overline{uv}|}{k} = a_1 = C_\mu f_\mu^n R\frac{S}{k} \tag{19}$$

where the turbulence structure parameter $a_1 = \sqrt{C_\mu}$. Recent DNS and experimental data indicate that this hypothesis is neither exactly valid in the viscous sublayer of the turbulent boundary layer nor in the free shear layers [6,7]. However, it is to be expected that the introduction of Eq. (19) with the one-equation model will actually lead to improved predictions of nonequilibrium flows [4]. Therefore, k may be determined from Eq. (19) as

$$k = \sqrt{C_\mu} R S f_\mu^{0.8} \tag{20}$$

where the exponent n of f_μ is chosen to be $n = 0.8$ to fit DNS and experimental data. Since $S \to 0$ away from the wall (i.e., freestream region), k given by Eq. (20) is insufficient there. In fact, the region where S is locally zero is bridged by the diffusion and convection terms in the k-ϵ turbulence model. With the assistance of [7], the mean strain rate correction S_α away from the wall is determined by numerical optimization:

$$S_\alpha = \frac{2C_\alpha f_\alpha}{3\nu}\left(\frac{\sqrt{u_i^2/2}}{1 + \mu_T/\mu}\right)^2 \tag{21}$$

with

$$C_\alpha = \sqrt{C_\mu^2 + \frac{\nu}{R + \nu}}, \qquad f_\alpha = 1 - \exp\left(-\frac{\mu_T}{36\mu}\right) \tag{22}$$

where $u_i = \sqrt{u^2 + v^2 + w^2}$ is the velocity magnitude and (u, v, w) is the velocity vector in Cartesian coordinates. Subsequently, the freestream corrections for k and ϵ can be calculated using S_α as follows:

$$k_\alpha = \nu S_\alpha, \qquad \epsilon_\alpha = \nu S_\alpha^2 \tag{23}$$

Note that since C_μ depends nonlinearly on both the shear and vorticity parameters, the structure parameter $a_1 = \sqrt{C_\mu}$ used in reconstructing k is no longer constant. However, the Bradshaw relation, Eq. (19), has no meaning for flows without shear. To extend the predictive capability, a modification is proposed to account for the effect of mean rotation rate on the mean strain rate:

$$\begin{aligned} \tilde{S} &= f_k\left(S - \frac{|\eta_1| - \eta_1}{C_T}\right), \qquad \eta_1 = S - W, \\ f_k &= 1 - \frac{f_\alpha}{C_T}\sqrt{\max(1 - Re, 0)} \end{aligned} \tag{24}$$

The advantage of this formulation is that k (and therefore, the turbulence eddy viscosity) is reduced in two regions: the region where the magnitude of the vorticity exceeds that of the strain rate (i.e., $Re > 1$), such as in the vortex core and the region with large values of η_1 (i.e., $Re < 1$) due to the appearance of f_k, such as around stagnation points. In principle, with $S \neq W$ Eq. (24) resembles the approach to enhancing the sensitivity of the turbulence model to streamline curvature that provokes an extra rate of strain in the flow field besides the main strain rate. Nevertheless, the overwhelming majority of applications of turbulence models is for shear dominated flows, where one-equation model is well suited. Thus, Eq. (20) can be reconstructed as follows:

$$k = \sqrt{\tilde{k}^2 + k_\alpha^2}, \qquad \tilde{k} = f_\mu^{0.8}\sqrt{C_\mu} R S_k, \qquad S_k = \sqrt{\tilde{S}^2 + S_\alpha^2} \tag{25}$$

The value of ϵ plays an important role in evaluating the realizable time scale T_t accompanied by the turbulence eddy viscosity μ_T, and is reconstructed as follows:

$$\epsilon = \sqrt{\epsilon_w^2 + \tilde{\epsilon}^2 + \epsilon_\alpha^2}, \qquad \tilde{\epsilon} = \frac{k^2}{R + \nu} \tag{26}$$

where $\tilde{\epsilon}$ unlike ϵ, vanishes at solid walls and ϵ_w signifies the wall-dissipation rate that equals to the viscous-diffusion rate [19], and is modeled as

$$\epsilon_w = 2A_\epsilon\nu\left(\frac{\partial u}{\partial y}\right)_w^2 \approx 2A_\epsilon\nu S_k^2 \tag{27}$$

where A_ϵ is a function of the Reynolds number. Experimental and DNS data of flat plate and channel flows indicate that $0.05 < A_\epsilon < 0.11$, with a preference for higher values at larger Reynolds numbers [17]. In the current work, $A_\epsilon = \tilde{C}_\mu = 0.09$ is adopted. Because of the inclusion of ν with Eq. (27), it seems likely that the contribution of ϵ_w to ϵ is confined within the wall layer.

III. Spalart–Allmaras Model

The SA model [3] is a transport equation model for the eddy viscosity. The differential equation is formulated using empirical criteria and arguments from dimensional analysis, Galilean invariance and selected dependence on the molecular viscosity. The SA model does not require a finer grid resolution than algebraic models do need to capture the velocity field gradients. A modified version of the SA model introduced by Spalart (see [20]) is considered in this study. The transport equation for the undamped eddy viscosity $\tilde{\nu}$ is given by

$$\frac{\partial \rho\tilde{\nu}}{\partial t} + \frac{\partial \rho u_j \tilde{\nu}}{\partial x_j} = \frac{\partial}{\partial x_j}\left[\left(\mu + \frac{\mu_T}{\sigma}\right)\frac{\partial \tilde{\nu}}{\partial x_j}\right] + c_{b1}\rho\tilde{W}\,\tilde{\nu} + c_{b2}\frac{\partial \tilde{\nu}}{\partial x_j}\frac{\partial \rho\tilde{\nu}}{\partial x_j} - c_{w1} f_w \rho\left(\frac{\tilde{\nu}}{y}\right)^2 \tag{28}$$

where y is the distance to the closest surface. The eddy viscosity is defined as

$$\mu_T = f_{v1}\rho\tilde{\nu}, \qquad f_{v1} = \frac{\chi^3}{\chi^3 + c_{v1}^3} \tag{29}$$

where $\chi = \tilde{\nu}/\nu$. This scheme allows $\tilde{\nu}$ to be equal to $\kappa y u_\tau$ in the log layer, buffer layer and viscous sublayer. This behavior is considered one of the reasons for the success of the SA model, since it enforces a numerically advantageous linear growth of $\tilde{\nu}$ in the vicinity of the wall. Recall that the damping function f_{v1} is important in the viscous region where χ is of $\emptyset(1)$, while its influence disappears in the logarithmic region.

The diffusion coefficient σ is modified such that sufficient diffusion is obtained in the vicinity of the wall:

$$\sigma = \tilde{C}_\mu + f_{v1} \tag{30}$$

The vorticity magnitude W is modified so that $\tilde{W}$ maintains its log-layer behavior, $\tilde{W} = u_\tau/(\kappa y)$:

$$\tilde{W} = W f_{v3} + \frac{\tilde{\nu}}{\kappa^2 y^2} f_{v2} \tag{31}$$

accomplished with the assistance of the functions

$$f_{v3} = \left(1 + \frac{\chi}{c_{v2}}\right)^{-3}, \qquad f_{v3} = \frac{(1+\chi f_{v1})(1 - f_{v2})}{\chi} \tag{32}$$

An efficient way for vanishing numerical problems is to take $\max(\chi, 10^{-4})$ instead of χ alone. The f_{v2} function remains positive along the wall and f_{v3} differs notably from 1 in the vicinity of walls. This results in a modification of the natural laminar-turbulent transition of the model [20]. The function f_w is used to obtain a faster decaying behavior of destruction in the outer region of the boundary layer:

$$f_w = q\left(\frac{1 + c_{w3}^6}{q^6 + c_{w3}^6}\right)^{1/6}, \qquad q = r + c_{w2}(r^6 - r), \qquad r = \frac{\tilde{\nu}}{\tilde{W}\kappa^2 y^2} \tag{33}$$

where q acts as a limiter that prevents large values of f_w. Both r and f_w achieve 1 in the log layer and decrease in the outer region. Constants of the model are: $c_{b1} = 0.1355$, $c_{b2} = 1.0$, $c_{v1} = 7.1$, $c_{v2} = 5.0$, $c_{w1} = 3.24$, $c_{w2} = 0.3$ and $c_{w3} = 2.0$.

Unlike the newly developed model, the SA model does not take k and ϵ into account to evaluate the eddy viscosity. However, they can be estimated using the Bradshaw relation and numerical optimization as documented in the previous section:

$$k = \sqrt{\tilde{k}^2 + k_\alpha^2}, \qquad \tilde{k} = \tilde{\nu} S_k (1 + \tilde{C}_\alpha^{0.8})\sqrt{f_{v1}/\tilde{C}_\mu}, \qquad \tilde{C}_\alpha = \sqrt{\tilde{C}_\mu^2 + 1/(1+\chi)^2} \tag{34}$$

$$\epsilon = \sqrt{\epsilon_w^2 + \tilde{\epsilon}^2 + \epsilon_\alpha^2}, \qquad \tilde{\epsilon} = f_{v1}^{1.3}\tilde{\nu} S_k^2 \tag{35}$$

Note that replacing C_α in Eq. (21) by $\tilde{C}_\alpha$, the associated parameters k_α, ϵ_α, ϵ_w and S_k can be evaluated from Eqs. (23), (24), and (27), respectively.

IV. Computations

To validate the generality and efficacy of the turbulence models, a few applications to two-dimensional turbulent flows consisting of fully developed channel flows, a backward facing step flow, an asymmetric plane diffuser flow, and a plane U-duct flow are considered. To convince the readers toward the model reliability and accuracy, the present model predictions are compared with those from the SA and Menter's shear stress transport (SST) k-ω [21] models. However, compared with the SA and SST models, the new model is additionally sensitized to nonequilibrium and anisotropic effects (i.e., anisotropic model coefficients, depending nonlinearly on both the rotational and irrotational strains).

A cell centered finite volume scheme combined with an artificial compressibility approach is employed to solve the flow equations [22–24]. A fully upwinded second-order spatial differencing is applied to approximate the convective terms. Roe's [25] damping term is used to calculate the flux on the cell face. A diagonally dominant alternating direction implicit time integration method [26] is applied for the iterative solution to the discretized equations. A multigrid method is used for the acceleration of convergence [27]. The basic implementation of the artificial compressibility method and associated features are described elsewhere [22–24]. Note that the elliptic relaxation Eq. (14) is solved using a tridiagonal matrix algorithm. In every coordinate direction, the implicit stage performs typically two sweeps that provide convincingly the converged state for f_μ at each iteration level. A variable grid spacing is used to resolve the sharp gradient in near-wall regions. Grid densities are varied to ensure the grid independence of numerical results.

A. Channel Flow

The computation is carried out for fully developed turbulent channel flows at $Re_\tau = 180$ and 395 for which turbulence quantities are attainable from the DNS data [17]. The calculation is conducted in the half-width of the channel, imposing periodic boundary conditions, except for the pressure, pertaining to the upstream and downstream boundaries. The computation involving a 96×64 nonuniform grid refinement is considered based on the grid independence test. For both cases, the length of the computational domain is 32δ, where δ is the channel half-width. To ensure the resolution of the viscous sublayer the first grid node near the wall is placed at $y^+ \approx 0.3$. Comparisons are made by plotting the results in the form of $u^+ = u/u_\tau$, $k^+ = k^+/u_\tau^2$, $\overline{uv}^+ = \overline{uv}/u_\tau^2$ and $\epsilon^+ = \nu\epsilon/u_\tau^4$ versus y^+.

Figure 2 shows the velocity profiles for different models. In this figure, the abbreviations $S1$ and $S2$ stand for the present models with the source terms $S_\lambda = (S_1, S_2)$ in Eq. (6), where $S_1 = \sqrt{P\tilde{R}}$ and $S_2 = PT_t$. The predictions of the $S1$ and $S2$ (present models) agree well with the SA and DNS data. Profiles of turbulent shear stresses are displayed in Fig. 3. Agreement of all model predictions with the DNS data seems to be satisfactory.

Further examination of the model performances is directed to the k^+ profiles as portrayed in Fig. 4 for the near-wall region. As is evident, the present and SA model predictions are in broad accord with the DNS data. Figure 5 exhibits the profiles of ϵ^+ from the three

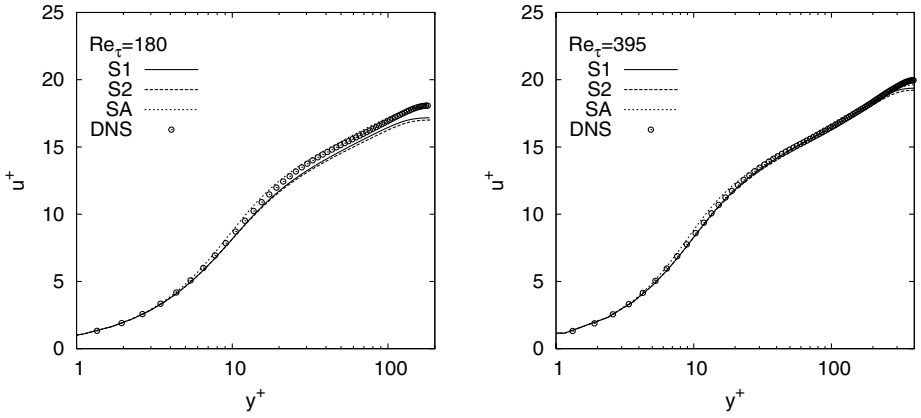

Fig. 2 Mean velocity profiles of channel flow.

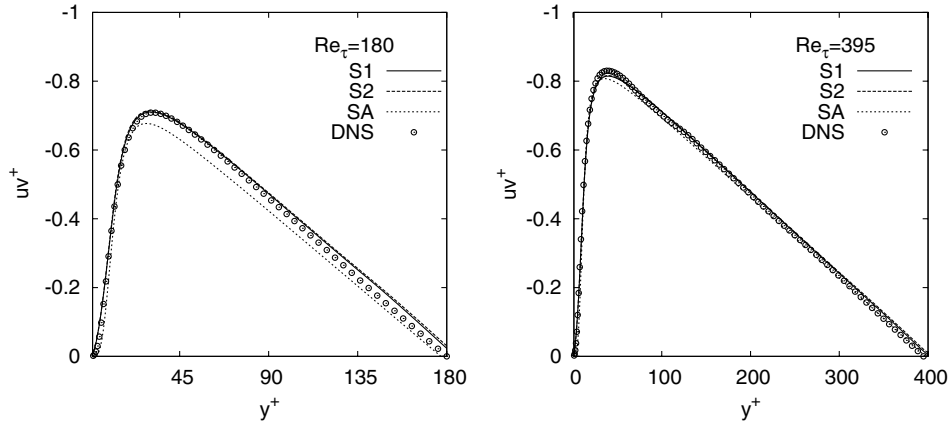

Fig. 3 Shear stress profiles of channel flow.

computations. All models provide a maximum ϵ^+ at the wall which is more in line with the experimental and DNS data.

B. Backward Facing Step Flow

To ascertain the performance in complex separated and reattaching turbulent flows, the models are applied to the flow over a backward facing step. The computations are conducted corresponding to the experimental case with zero deflection of the wall opposite to the step, as investigated by Driver and Seegmiller [28]. The reference velocity $U_{\text{ref}} = 44.2$ m/s and the step height $h = 0.0127$ m. The ratio between the channel height and the step height is 9, and the step height Reynolds number is $Re = 3.75 \times 10^4$. At the channel inlet, the Reynolds number based on the momentum thickness is $Re_\theta = 5.0 \times 10^4$.

For the computations, grids are arranged in two blocks. The smaller one (extended from the inlet to the step) contains a 16×48 nonuniform grid and the grid size for other one is 120×80. The maximum height of the first near-wall grid node is at $y^+ < 1.5$. The inlet conditions are specified four step heights upstream of the step corner and the outlet boundary conditions are imposed 30 step heights downstream of the step corner. The inlet profiles for all dependent variables are generated by solving the models at the appropriate momentum thickness Reynolds number. Profiles of mean velocity, shear stress and turbulent kinetic energy at the inlet are presented in Fig. 6. All models ensure close adherence to the experimental data. All the quantities shown along the x or y axis are normalized by the step height h and the experimental reference freestream velocity U_{ref}, provided that the distance x/h is measured exactly from the step corner.

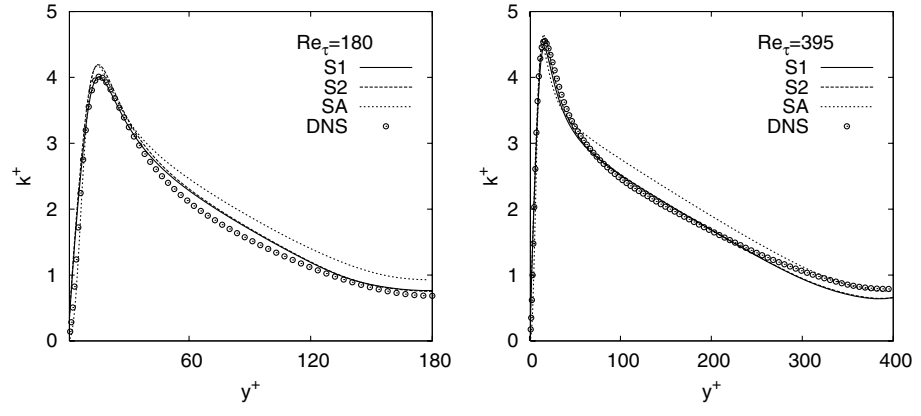

Fig. 4 Turbulence kinetic energy profiles of channel flow.

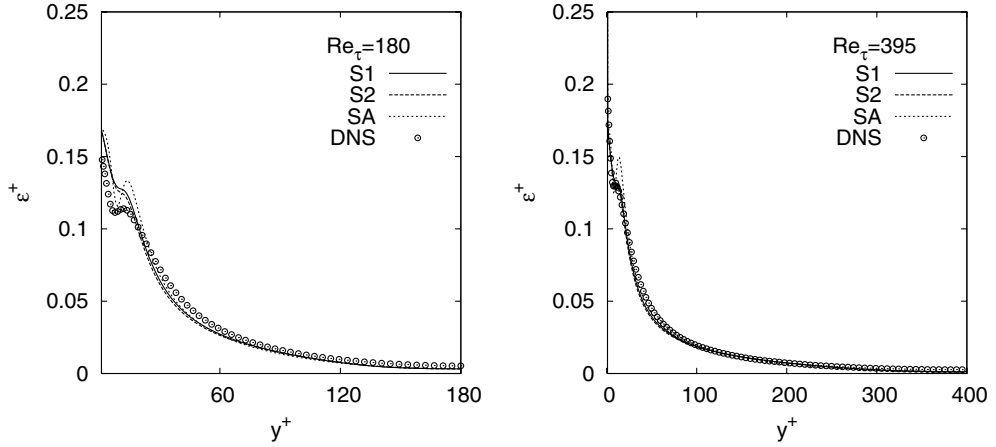

Fig. 5 Dissipation rate profiles of channel flow.

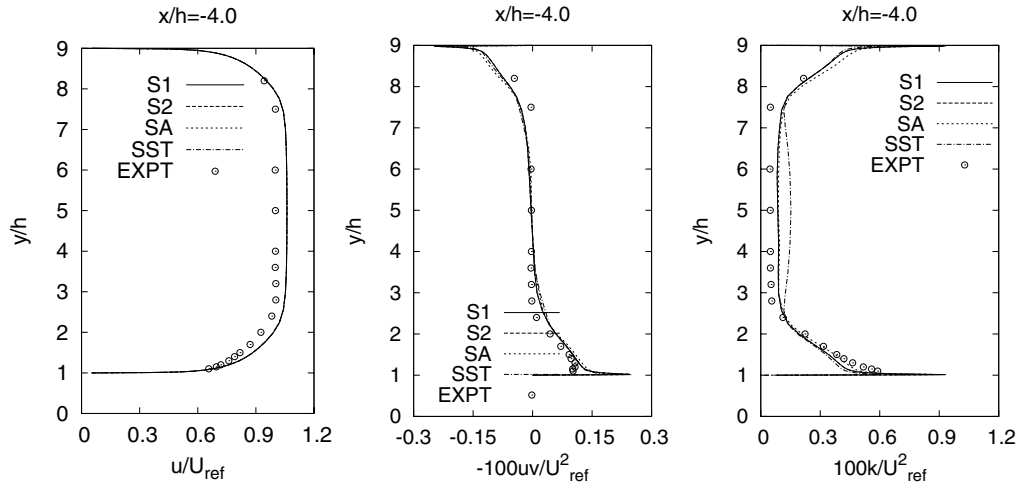

Fig. 6 Inlet profiles for step flow.

Computed and experimental friction coefficients ($C_f = 2u_\tau^2/U_{\text{ref}}^2$) along the stepside wall are plotted in Fig. 7. As is observed, all models are in good agreement with the data. However, the present model slightly overpredicts the C_f profile in the recovery region. The positive C_f that starts from $x/h = 0$ is due to a secondary eddy which sits in the corner at the base of the step, inside the main recirculation region. The recirculation lengths predicted by the present ($S1$ and $S2$), SA, and SST models are $6.4h$, $6.2h$, and $6.5h$, respectively. The experimental value of the reattachment length is $(6.26 \pm 0.1)h$, making a fairly good correspondence with the models. A closer inspection of the C_f distribution indicates that $S1$ and $S2$ differ slightly from each other in the recovery region.

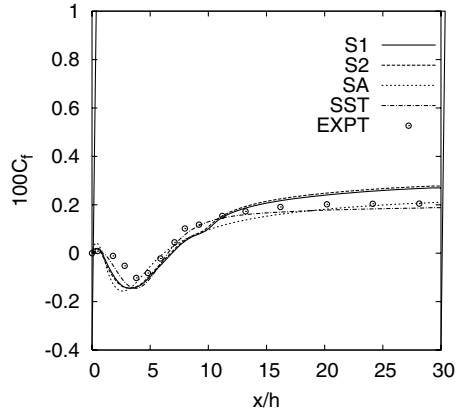

Fig. 7 Skin friction coefficient along the stepside bottom wall.

The streamwise mean velocity profiles at three representative positions are depicted in Fig. 8. Obviously, the predictions of all models are in good agreement with the experiment. Comparisons are extended to the distributions of the Reynods shear stress and the corresponding turbulent kinetic energy at different x/h locations behind the step corner, as shown in Figs. 9 and 10. Since the $\overline{ww}$ component is not measured in the experiment, the usual approximation $k \approx 3/4(\overline{uu} + \overline{vv})$ is employed. A closer inspection of the distribution indicates that the present and SA model predictions are in a broad agreement with the SST and experimental data. On average, the agreement of present model with the data is better than that of the SA model.

C. Asymmetric Plane Diffuser Flow

To validate the performance in complex separated and reattaching turbulent flows, the models are further applied to the flow in an asymmetric diffuser with an opening angle of 10°, for which measurements are available [29]. The expansion ratio of 4.7 is sufficient to produce a separation bubble on the deflected wall. Hence the configuration provides a test case for smooth, adverse pressure driven separation. The entrance to the diffuser consists of a plane channel to invoke fully developed flow with $Re = 2.0 \times 10^4$ based on the centerline velocity U_{ref} and the inlet channel height h. The length of the computational domain is $76h$. Profiles of mean velocity, shear stress and turbulent kinetic energy at the inlet are presented in Fig. 11. All models ensure close resemblance with the experimental data.

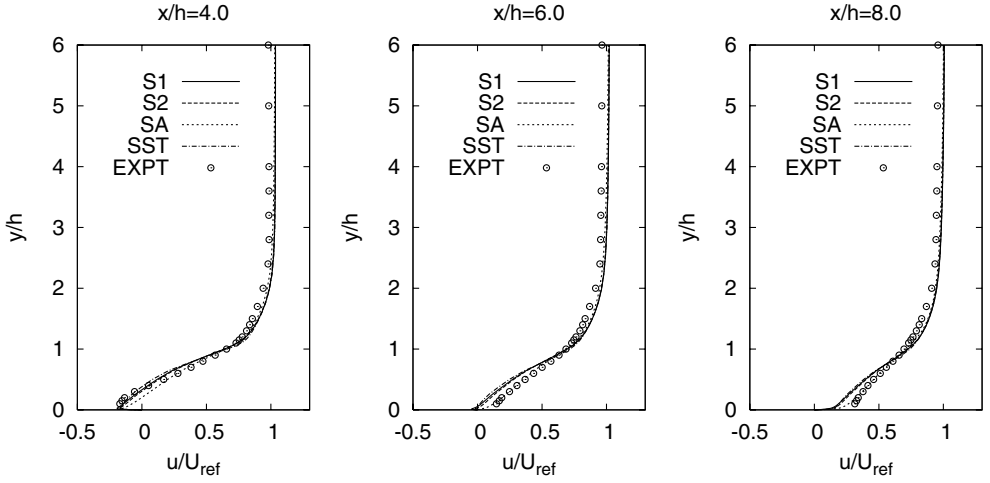

Fig. 8 Mean velocity profiles at selected locations for step flow.

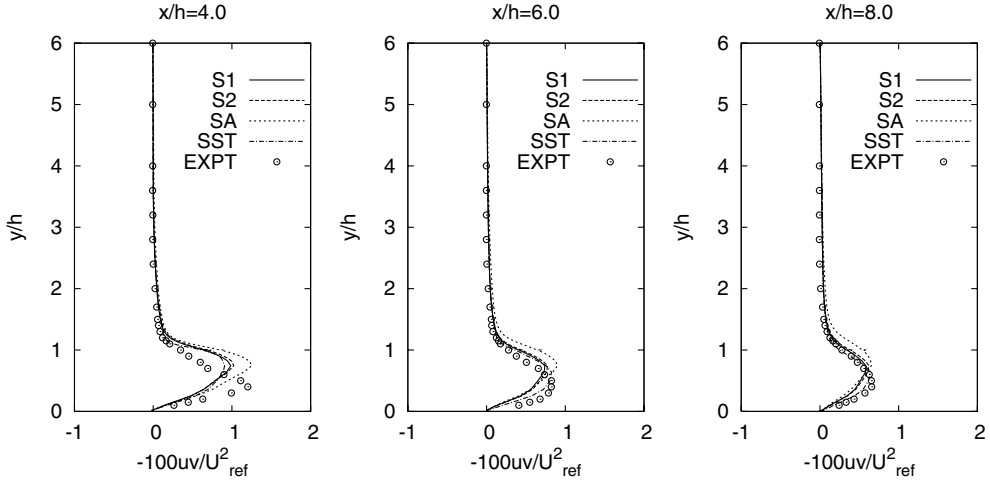

Fig. 9 Shear stress profiles at selected locations for step flow.

Figure 12 shows the skin friction coefficient using the S_2 turbulence model on two grids. Except outside the separated flow region, there is very little difference between the coarse (60×36) and fine grid (120×72) results. Other turbulence models show similar/smaller grid sensitivities. Therefore, computations involving a 120×72 nonuniform grid resolution are considered to be accurate to describe the flow characteristics. The thickness of the first cell remains below one in y^+ unit on both the deflected and flat walls.

Figure 13 portrays the predicted skin friction coefficients. The performance of the present ($S1$ and $S2$) and SA models evince an encouraging qualitative agreement with the SST model and measurements. As is observed, the SST model perform significantly

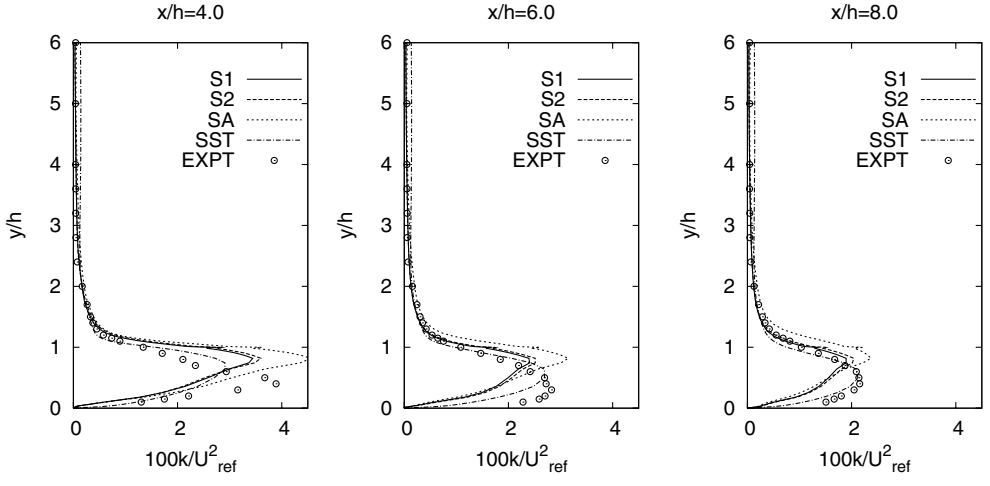

Fig. 10 Kinetic energy profiles at selected locations for step flow.

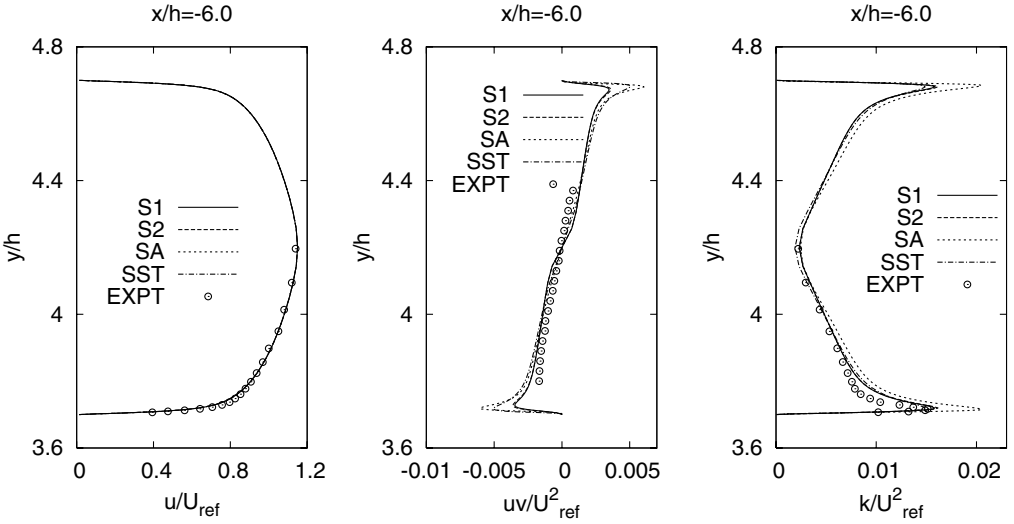

Fig. 11 Inlet profiles for diffuser flow.

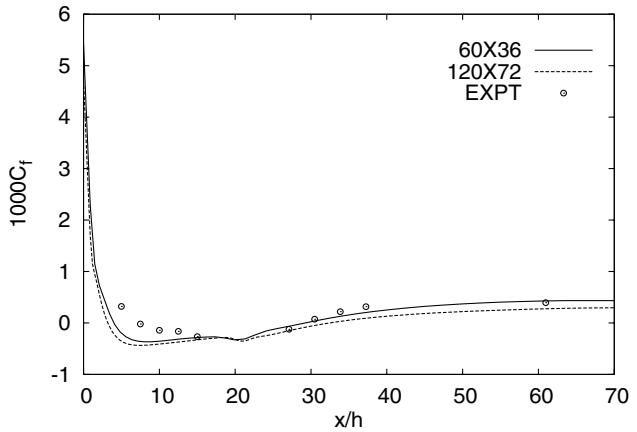

Fig. 12 Effect of grid density on skin friction coefficient of diffuser flow along the deflected bottom wall using S_2 model.

better than other models. The present model predicts the C_f profile (along the straight top wall) better than the SA model.

Figure 14 exhibits the mean velocity profiles at three representative positions. The performance of all present models in predicting the velocity profiles is distinguishable. Unlike the SA model, the present model predicts some anisotropy of turbulence due to the variation of C_μ in the eddy viscosity formulation, and hence yields results in better agreement with the data. Compared with the experiment, the SA model tend to gradually underpredict the peak for u profile toward the outlet of the diffuser. Comparisons are extended to the distributions of Reynolds shear stress and the corresponding turbulent kinetic energy at different x/h locations, as displayed in Figs. 15 and 16. Since the $\overline{ww}$ component is not measured in the experiment, the usual approximation $k \approx 3/4(\overline{uu} + \overline{vv})$ is employed. A closer inspection of the distribution indicates that the present and SA model predictions are in a broad agreement with the experimental data. However, the SST model has the best agreement with the measured data for u, uv and k profiles.

D. Plane U-Duct Flow

To further evaluate the performance, the models are applied to simulate the flow in a plane U-duct with strong streamline curvature effects. The computations are conducted corresponding to the experimental case with $Re = 10^6$, based on the channel height $h = 3.81$ cm and reference velocity $U_{\text{ref}} = 31.8$ m/s [30,31]. The turn has an inner radius of $r_i = 1.91$ cm and an outer radius of $r_o = 5.72$ cm. The finest grid employed is 288×160 and extends from $x/h = -4$ upstream of the bend to $x/h = 12$ downstream. The maximum height of the first near-wall grid node is at $y^+ < 1.0$. The computational grid is shown in Fig. 17. The inlet boundary conditions are approximated from the experimental data, as depicted in Fig. 18. A coarser grid 144×80 is used to investigate grid sensitivity. However, no significant differences are found between the coarse and fine grid results as can be seen from Fig. 19. Other turbulence models produce analogous grid-sensitivity results.

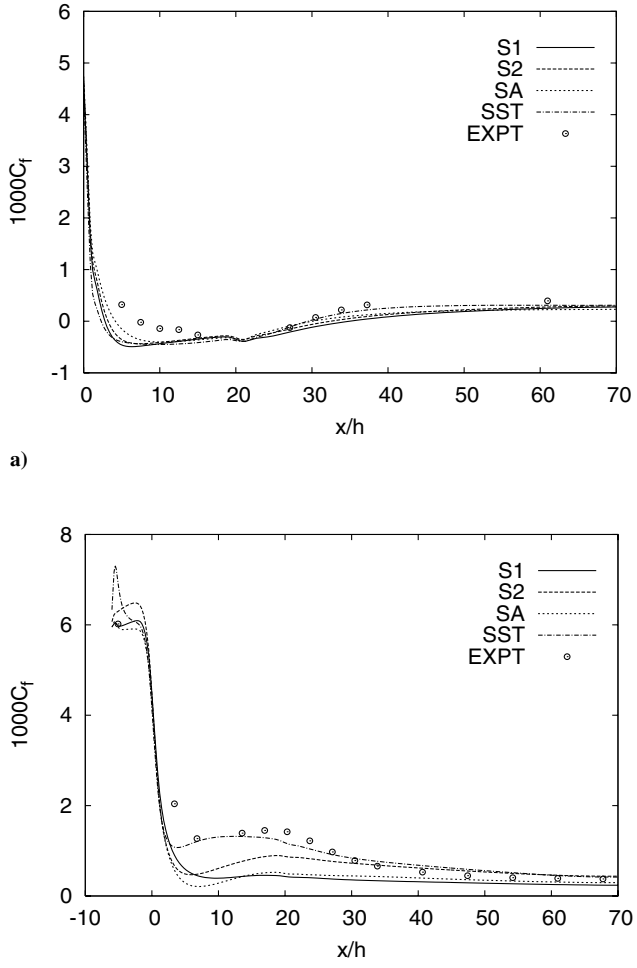

Fig. 13 Skin friction coefficients of diffuser flow: a) along the deflected bottom wall and b) along the straight top wall.

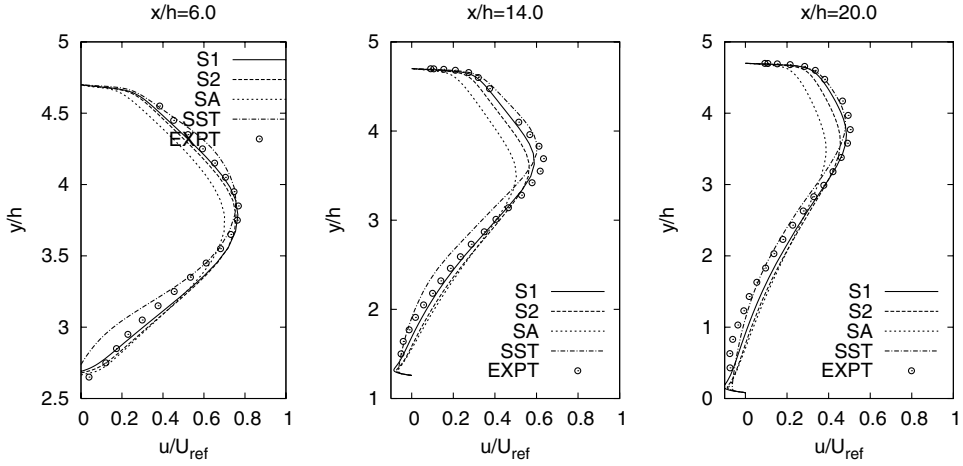

Fig. 14 Mean velocity profiles at selected locations for diffuser flow.

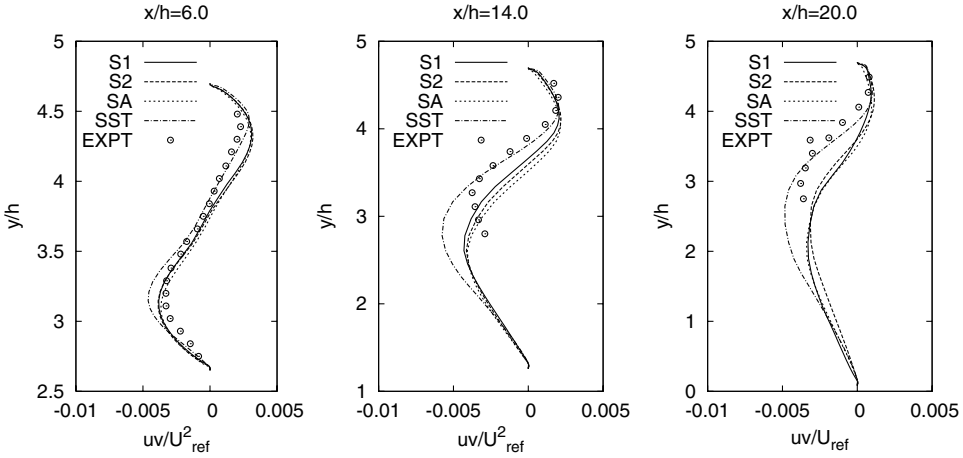

Fig. 15 Shear stress profiles at selected locations for diffuser flow.

The predicted and experimental profiles of the streamwise velocity, shear stress and turbulent kinetic energy are shown in Figs. 20–22, respectively. At station $\theta = 0^\circ$ ($x/h = 0$, where the bend begins), all models predict the mean velocity in good agreement with each other and with experiment. The flow undergoes rapid acceleration near the inner wall and deceleration near the outer wall. The curvature effect on turbulence can be clearly observed from the experimental data. The convex curvature together with a large flow acceleration strongly attenuates the turbulence shear stress and kinetic energy near the inner wall. Comparing with the present and

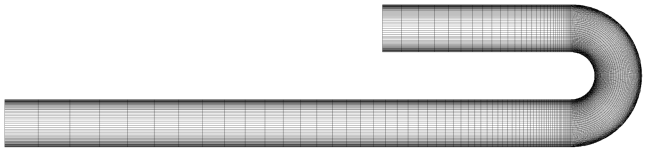

Fig. 17 Computational grid for U-duct flow.

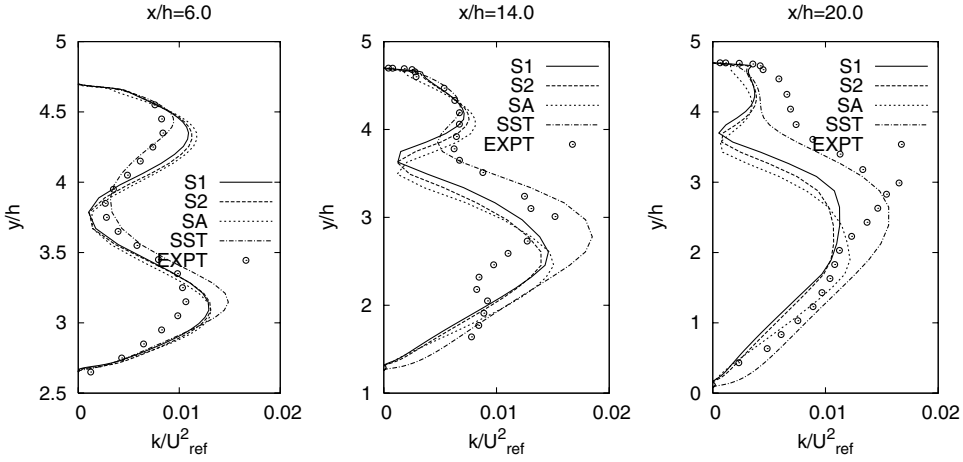

Fig. 16 Kinetic energy profiles at selected locations for diffuser flow.

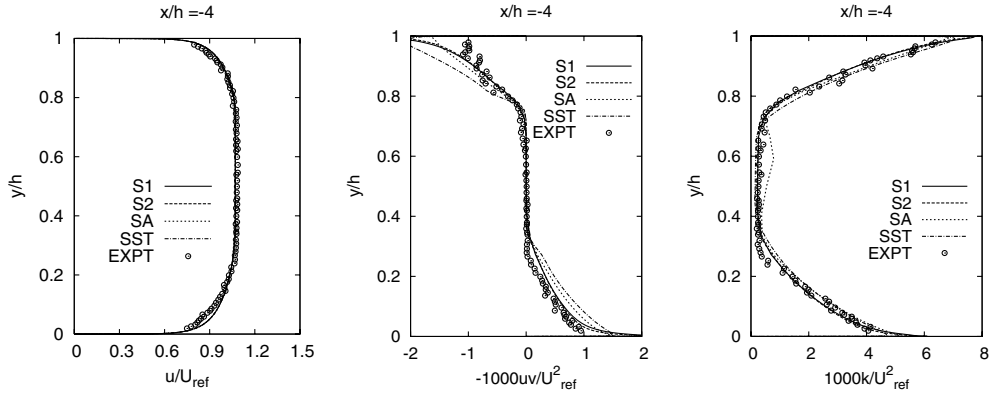

Fig. 18 Profiles at inlet for U-duct flow.

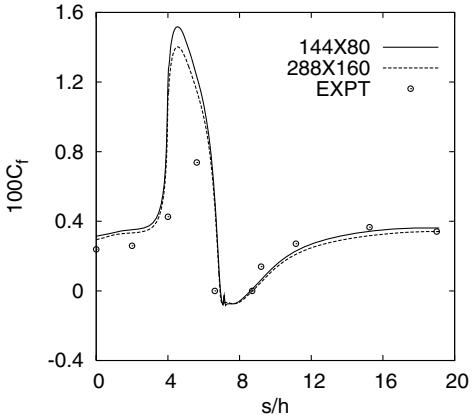

Fig. 19 Effect of grid density on inner surface skin friction coefficient of U-duct flow using S_2 model.

SST models, the SA model overpredict the magnitude of $-\overline{uv}$ significantly near the convex/concave wall. For the kinetic energy profiles, all models yield good results that agree with the measured data to some extent.

As the flow reaches the $\theta = 90^\circ$ position halfway around the bend, the curvature of the bend affects the turbulence significantly. The turbulence is damped near the convex wall, whereas turbulence enhancement occurs near the concave wall. All models predict similar velocity profiles having reasonable agreement with experiment, although the velocity magnitude near the outer wall is underpredicted. None of the models is actively sensitive to the curvature effect, overpredicting/underpredicting the shear stress and kinetic energy levels at the convex/concave surface. In strong contrast, the present $S2$ model with a variable C_μ shows improved predictions of $-\overline{uv}$ and k near both walls, in better agreement with the experiment.

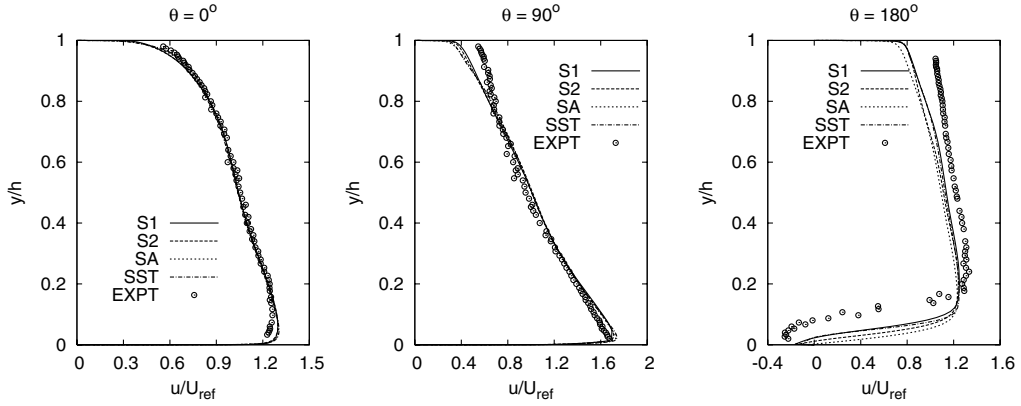

Fig. 20 Velocity profiles at selected locations for U-duct flow.

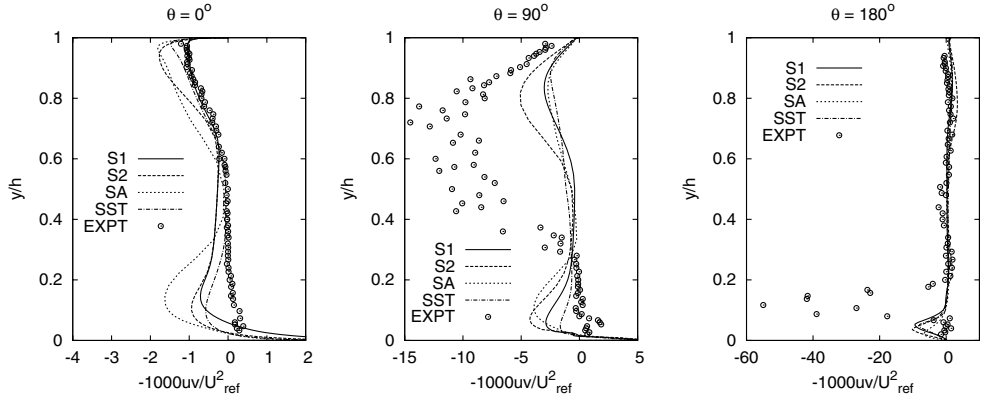

Fig. 21 Shear stress profiles at selected locations for U-duct flow.

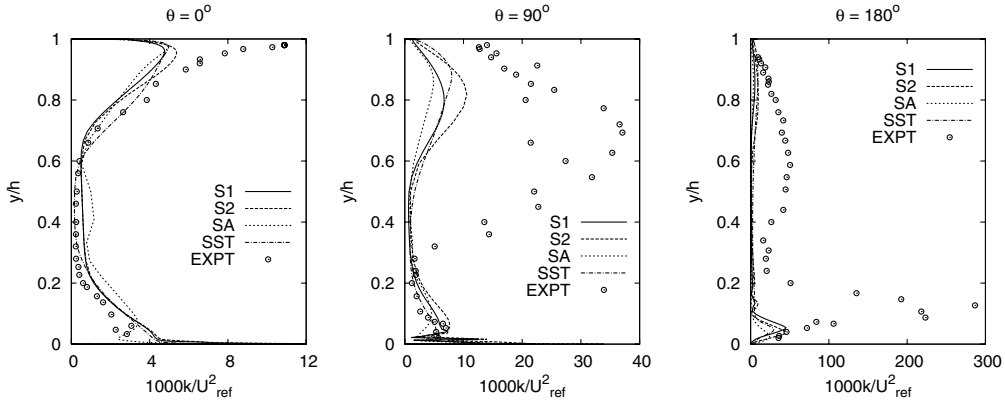

Fig. 22 Kinetic energy profiles at selected locations for U-duct flow.

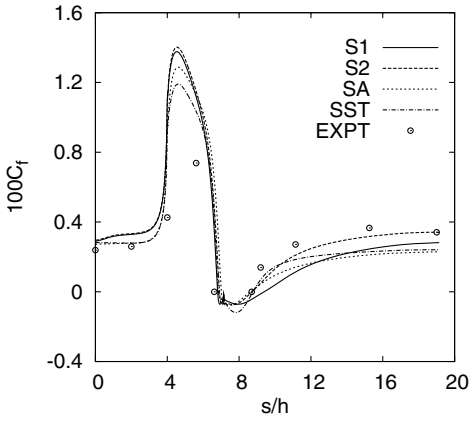

Fig. 23 Inner surface skin friction coefficient for U-duct flow.

In fact, the flow envisages an adverse pressure gradient on the inner wall and a favorable pressure gradient on the outer wall downstream of $\theta = 90°$ [32]. Because of the severe adverse pressure gradient, as well as highly diminished turbulent shear stress, the boundary layer separates in the experiment around $\theta = 150°$ on the convex wall and extends to $x/h = 1.0 - 1.5$ downstream of the end of bend. The velocity profiles predicted by the present, SA, and SST models at station $\theta = 180°$ agree well with the data. Nevertheless, there is a remarkable discrepancy between the numerical and experimental results in the turbulence quantities at the end of bend. The measured data show a very strong peak in the turbulent kinetic energy and shear stress profiles at the convex surface, which is not captured by any model. This large peak values probably result from large unsteadiness of the separation bubble, as reported in the experiment.

Computed and experimental friction coefficients C_f on the inner wall are plotted in Fig. 23. The s signifies the distance of the channel centerline from the U-duct inlet. As is observed, the present $S2$, SA, and SST model results are close to those of experimental data. They nearly capture the separation and reattachment points, having comparable separation lengths in good agreement with the data. However, the glaring discrepancy is that the SA and SST models fail to recover the downstream experimental values in contrast to the present $S2$ model and the C_f is best predicted by the $S2$ model. The static pressure coefficient C_p along the inner wall is shown in Fig. 24. On average, all models predict the pressure level downstream of the bend in good agreement with the experiment.

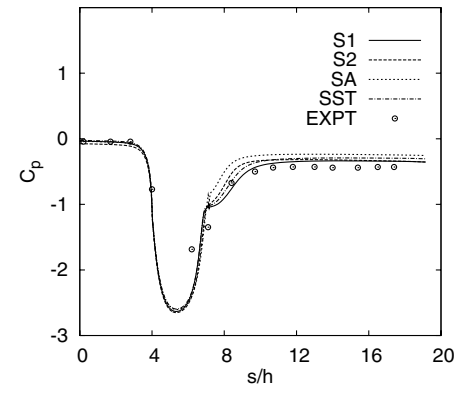

Fig. 24 Inner surface pressure coefficient for U-duct flow.

V. Conclusions

The new turbulence model accounts for the near-wall and LRN effects issuing from the physical requirements. The R-transport equation having two different source terms replicates analogous results, except with the U-duct flow. The eddy viscosity formulation depends nonlinearly on both the mean strain rate and vorticity invariants, and ensures realizability. The anisotropic production in the R equation is accounted for substantially by modifying the model coefficients $C_{1,2}$, leading to a reduced level of turbulence generation in nonequilibrium flow regions. Consequently, the model is capable of evaluating the flow cases with separation and reattachment. Contrasting the predicted results with measurements demonstrates that the present model is a significant improvement over the constant C_μ model such as the SA model and turns out to be competitive with the SST k-ω model. The proposed model is wall distance free, tensorially invariant, frame-indifferent and applicable to arbitrary topology in conjunction with structured/unstructured grids. The performance evaluation dictates that the present $S2$ model may be the best choice for engineering applications. In addition, the $S2$ model can easily be extended to a nonlinear eddy viscosity model.

References

[1] Baldwin, B. S., and Lomax, H., "Thin Layer Approximation and Algebraic Model for Separated Turbulent Flows," AIAA Paper 78-257, 1978.

[2] Baldwin, B. S., and Barth, T. J., "A One-Equation Turbulence Transport Model for High-Reynolds Number Wall-Bounded Flows," NASA TM-102847, 1990.

[3] Spalart, P. R., and Allmaras, S. R., "A One-Equation Turbulence Model for Aerodynamic Flows," AIAA Paper 92-0439, 1992.

[4] Menter, F. R., "Eddy Viscosity Transport Equations and Their Relation to the k-ϵ Model," *Journal of Fluids Engineering*, Vol. 119, No. 4, 1997, pp. 876–884. doi:10.1115/1.2819511

[5] Elkhoury, M., "Assessment and Modification of One-Equation Models of Turbulence for Wall-Bounded Flows," *Journal of Fluids Engineering*, Vol. 129, No. 7, 2007, pp. 921–928. doi:10.1115/1.2743666

[6] Fares, E., and Schröder, W., "A General One-Equation Turbulence Model for Free Shear and Wall-Bounded Flows," *Flow, Turbulence and Combustion*, Vol. 73, Nos. 3–4, 2005, pp. 187–215. doi:10.1007/s10494-005-8625-y

[7] Nagano, Y., Pei, C. Q., and Hattori, H., "A New Low-Reynolds-Number One-Equation Model of Turbulence," *Flow, Turbulence and Combustion*, Vol. 63, Nos. 1–4, 2000, pp. 135–151. doi:10.1023/A:1009924002401

[8] Bradshaw, P., Ferriss, D. H., and Atwell, N. P., "Calculation of Boundary Layer Development Using the Turbulent Energy Equation," *Journal of Fluid Mechanics*, Vol. 28, No. 3, 1967, pp. 593–616.

[9] Rahman, M. M., and Siikonen, T., "Modifications for an Explicit Algebraic Stress Model," *International Journal for Numerical Methods in Fluids*, Vol. 35, No. 2, 2001, pp. 221–245. doi:10.1002/1097-0363(20010130)35:2<221::AID-FLD93>3.0.CO;2-N

[10] Pope, S. B., "A More General Effective Viscosity Hypothesis," *Journal of Fluid Mechanics*, Vol. 72, No. 2, 1975, pp. 331–340. doi:10.1017/S0022112075003382

[11] Gatski, T. B., and Speziale, C. G., "On the Explicit Algebraic Stress Models for Complex Turbulent Flows," *Journal of Fluid Mechanics*, Vol. 254, No. 1, 1993, pp. 59–78. doi:10.1017/S0022112093002034

[12] Lumley, J. L., "Computational Modeling of Turbulent Flows," *Advances in Applied Mechanics*, Vol. 18, 1978, pp. 124–176.

[13] Rahman, M. M., and Siikonen, T., "An Eddy Viscosity Model with Near-Wall Modifications," *International Journal for Numerical Methods in Fluids*, Vol. 49, No. 9, 2005, pp. 975–997. doi:10.1002/fld.1034

[14] Manceau, R., Wang, M., and Laurence, D., "Inhomogeneity and Anisotropy Effects on the Redistribution Term in Reynolds-Averaged Navier–Stokes Modelling," *Journal of Fluid Mechanics*, Vol. 438, July 2001, pp. 307–338.

[15] Durbin, P. A., "Near-Wall Turbulence Closure Modeling Without Damping Functions," *Theoretical and Computational Fluid Dynamics*, Vol. 3, No. 1, 1991, pp. 1–13.

[16] Rahman, M. M., and Siikonen, T., "An Eddy Viscosity Model with Elliptic Relaxation Approach," *International Journal of Heat and Fluid Flow*, Vol. 30, No. 2, 2009, pp. 319–330. doi:10.1016/j.ijheatfluidflow.2008.12.012

[17] Mansour, N. N., Kim, J., and Moin, P., "Reynolds-Stress and Dissipation-Rate Budgets in a Turbulent Channel Flow," *Journal of Fluid Mechanics*, Vol. 194, No. 1, 1998, pp. 15–44. doi:10.1017/S0022112088002885

[18] Durbin, P. A., "A Reynolds-Stress Model for Near-Wall Turbulence," *Journal of Fluid Mechanics* Vol. 249, No. 1, 1993, pp. 465–498. doi:10.1017/S0022112093001259

[19] Patel, V. C., Rodi, W., and Scheuerer, G., "Turbulence Models for Near-Wall and Low Reynolds Number Flow: A Review," *AIAA Journal*, Vol. 23, No. 9, 1985, pp. 1308–1319. doi:10.2514/3.9086

[20] Deck, S., Duveau, P., d'Espiney, P., and Guillen, P., "Development and Application of Spalart–Allmaras One Equation Turbulence Model to Three-Dimensional Supersonic Complex Configurations," *Aerospace Science and Technology*, Vol. 6, No. 3, 2002, pp. 171–183. doi:10.1016/S1270-9638(02)01148-3

[21] Menter, F. R., "Two-Equation Eddy-Viscosity Turbulence Models for Engineering Applications," *AIAA Journal*, Vol. 32, No. 8, 1994, pp. 1598–1605. doi:10.2514/3.12149

[22] Rahman, M. M., Rautaheimo, P., and Siikonen, T., "Numerical Study of Turbulent Heat Transfer from a Confined Impinging Jet Using a Pseudo-Compressibility Method," *Second International Symposium on Turbulence, Heat and Mass Transfer*, edited by K. Hanjalic and T. W. J. Peeters, Delft Univ. Press, Delft, The Netherlands, 1997, pp. 511–520.

[23] Rahman, M. M., and Siikonen, T., "An Artificial Compressibility Method for Incompressible Flows," *Numerical Heat Transfer, Part B, Fundamentals*, Vol. 40, No. 5, 2001, pp. 391–409. doi:10.1080/104077901753243188

[24] Rahman, M. M., and Siikonen, T., "An Artificial Compressibility Method for Viscous Incompressible and Low Mach Number Flows," *International Journal for Numerical Methods in Engineering*, Vol. 75, No. 11, 2008, pp. 1320–1340. doi:10.1002/nme.2302

[25] Roe, P. L., "Approximate Riemann Solvers, Parameter Vectors, and Difference Schemes," *Journal of Computational Physics*, Vol. 43, No. 2, 1981, pp. 357–372. doi:10.1016/0021-9991(81)90128-5

[26] Lombard, C., Bardina, J., Venkatapathy, E. J., and Oliger, J., "Multi-Dimensional Formulation of CSCM: An Upwind Flux Difference Eigenvector Split Method for the Compressible Navier–Stokes Equations," *6th AIAA Computational Fluid Dynamics Conference*, pp. 649–664; also AIAA Paper 1983-1895-CP, 1983.

[27] Jameson, A., and Yoon, S., "Multigrid Solution of the Euler Equations Using Implicit Schemes," *AIAA Journal*, Vol. 24, No. 11, 1986, pp. 1737–1743. doi:10.2514/3.9518

[28] Driver, D. M., and Seegmiller, H. L., "Features of a Reattaching Turbulent Shear Layer in Divergent Channel Flow," *AIAA Journal*, Vol. 23, No. 2, 1985, pp. 163–171. doi:10.2514/3.8890

[29] Buice, C., and Eaton, J. K., "Experimental Investigation of Flow Through an Asymmetric Plane Diffuser," Stanford Univ., Dept. of Mechanical Engineering, Thermoscience Div., Stanford Univ. Rept. TSD-107, Palo Alto, CA, 1997.

[30] Monson, D. J., Seegmiller, H. L., McConnaughey, P. K., and Chen, Y. S., "Comparison of Experiment with Calculations Using Curvature-Corrected Zero and Two-Equation Turbulence Models for a Two-Dimensional U-Duct," AIAA Paper 90-1484, 1990.

[31] Monson, D. J., and Seegmiller, H. L., "An Experimental Investigation of Subsonic flow in a Two-Dimensional U-Duct," NASA TM 103931, 1992.

[32] Luo, J., and Lakshminarayana, B., "Prediction of Strongly Curved Turbulent Duct Flows with Reynolds Stress Model," *AIAA Journal*, Vol. 35, No. 1, 1997, pp. 91–98. doi:10.2514/2.67

B. Balachandran
Associate Editor